Analysis and Design of Checkerboard Leaky-Wave Antennas With Low Radar Cross Section

SUBRAMANIAN RAMALINGAM (Member, IEEE), **CONSTANTINE A. BALANIS** (Life Fellow, IEEE),
CRAIG R. BIRTCHER, AND SIVASEETHARAMAN PANDI (Member, IEEE)

School of Electrical, Computer, and Energy Engineering, Arizona State University, Tempe, AZ 85287, USA

CORRESPONDING AUTHOR: C. A. BALANIS (e-mail: balanis@asu.edu)

ABSTRACT This paper addresses the analysis and design of a new class of metasurface leaky-wave antennas (LWAs) that inherently have low monostatic radar cross section (RCS) for normal incidence parallel polarization. The impedance profile of these antennas is modulated with a square wave to achieve leaky-wave behavior with low RCS. The low RCS performance is justified by the concepts of generalized Snell's law of reflection and array theory. When the reflection phase difference between consecutive periods is near 180°, the power reflected in the specular direction is minimal. It is also shown that modulating the surface impedance with a square wave still results in a high-gain fan beam similar to that of a sinusoidal modulation; however, the trade-off for obtaining a low RCS is an increase in the sidelobe level due to radiation from higher-order harmonics. A similar trade-off exists between the gain/beamwidth and RCS reduction. A prototype of an LWA with low RCS was fabricated and measured; an excellent agreement was observed between simulations and measurements.

INDEX TERMS Anomalous reflection, checkerboard surfaces, diffraction grating, diffraction modes, generalized Snell's law, impedance modulation, leaky waves, leaky-wave antennas, metasurfaces.

I. INTRODUCTION

METASURFACE leaky-wave antennas (LWAs) are radiating structures with thin and light-weight geometries that are characterized by high gains and narrow beamwidths [1]. LWAs has been an attractive topic ever since the high gain from sinusoidally-modulated impedance surfaces was interpreted using leaky waves in [2]. LWAs have also been examined for their frequency-scanning abilities and sidelobe levels [3]. These metasurface antennas can be used for space, imaging and automotive radar applications [4]–[6]. One-dimensionally (1-D) periodic metasurface LWAs were realized in [7], while two-dimensionally (2-D) periodic metasurface LWAs were examined and characterized in [4], [8]–[12]. The need to flush-mount these antennas on vehicles has motivated research on conformal antennas, which for cylindrically-curved conformal LWAs were reported in [5], [13]–[15]. Leaky-wave concepts have also been used to achieve a perfect anomalous reflection [16] and to explain Wood's anomalies [17].

Low-RCS antennas are necessary for scattering applications. The existing techniques to reduce the RCS of antennas employ metasurfaces, perfect absorber metamaterials

(PAMs), frequency selective surfaces (FSSs) and artificial magnetic conductors (AMCs) around the radiating elements [18]–[21]. However, the implementation of such techniques for metasurface LWAs increases the overall size (area) of the radiating structure, as shown in Fig. 1a.

In some designs, these meta-structures are also implemented as a substrate or ground plane for the radiating element [22], [23]; this might not apply to impedance-modulated metasurface leaky-wave antennas. Some designs of low-RCS antennas include electromagnetic band-gap structures (EBGs), partially reflecting surfaces (PRSs) and metasurfaces as superstrates [24]–[29]. However, these techniques result in an increased thickness of the radiating system.

This paper intrinsically reduces the monostatic RCS of the metasurface LWAs, for normal incidence parallel polarization, without increasing the overall size or thickness of the radiating structure. RCS reduction is achieved by modulating the surface impedance with a square-wave, in lieu of a sinusoidal, as illustrated in Fig. 1b. The square-wave modulation is inspired by checkerboard metasurfaces that are popular for RCS reduction [30]. These metasurfaces
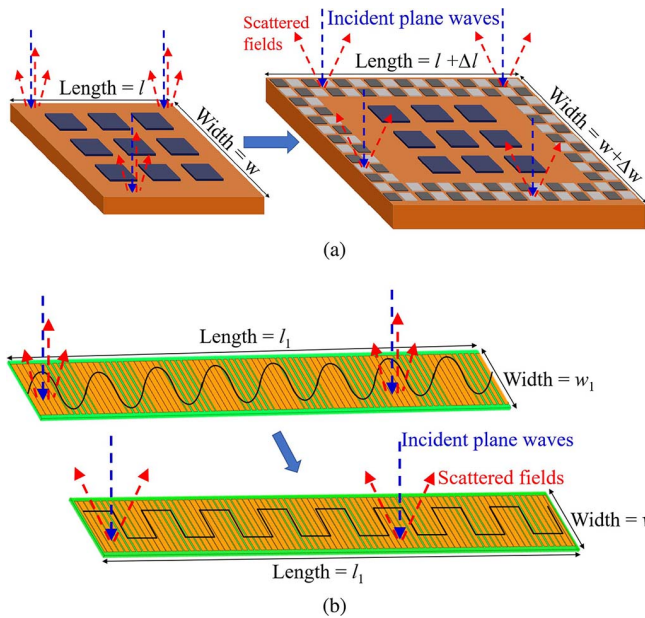
FIGURE 1. (a) The existing technique to reduce the RCS of antennas, where the radiating elements are surrounded by metasurfaces. This increases the overall size of the structure. (b) The proposed low-RCS metasurface leaky-wave antenna, where the RCS is intrinsically reduced without increasing the size or thickness of the structure.
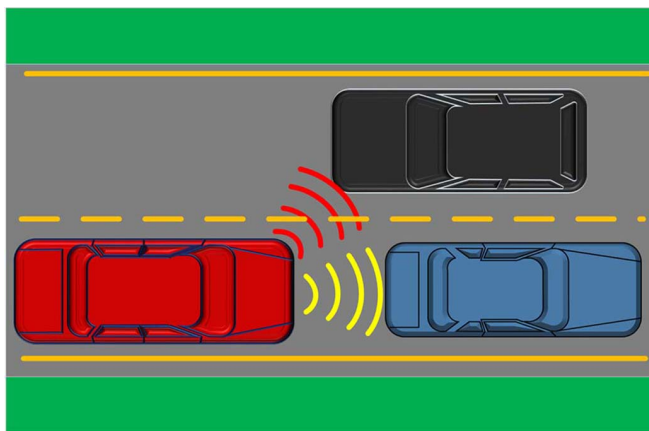

FIGURE 2. Automotive radar technology for driver assistance and safety.

are realized by arranging metallic patches and AMCs in a checkerboard pattern. As AMCs mimic perfect magnetic conductors (PMCs) at a particular (resonant) frequency, a progressive reflection phase difference of 180° is realized in the structure. This reflection phase difference scatters the beam away from the specular direction, based on the generalized Snell's law of reflection and, hence, achieves RCS reduction along the specular direction.

Low-RCS antennas can be utilized in automotive radar technology, which is popular for driver assistance and safety. High-gain beam-steering antennas are desired for features like collision avoidance and lane change assistance, as illustrated in Fig. 2. Currently, this technology predominantly uses phased arrays. However, metasurface LWAs are light, geometrically thin, and do not need complex feeds, making
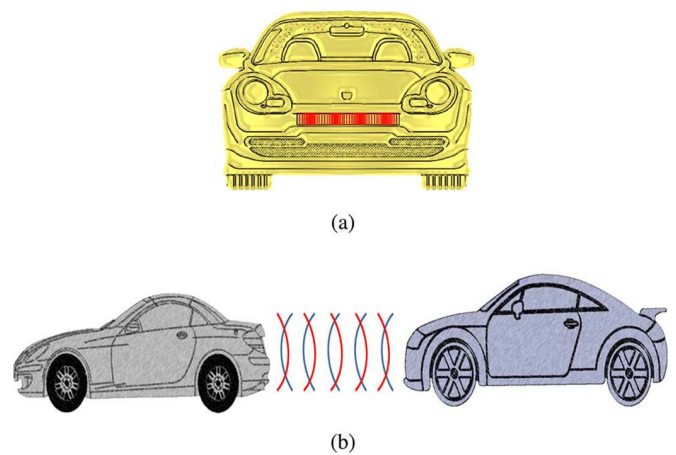

FIGURE 3. (a) A metasurface LWA, shown in red, employed on a car for automotive radar applications. (b) Multiple reflections between the target (car in front) and the antenna. Standing waves are formed by the transmitted waves shown in blue and the reflected ones shown in red.
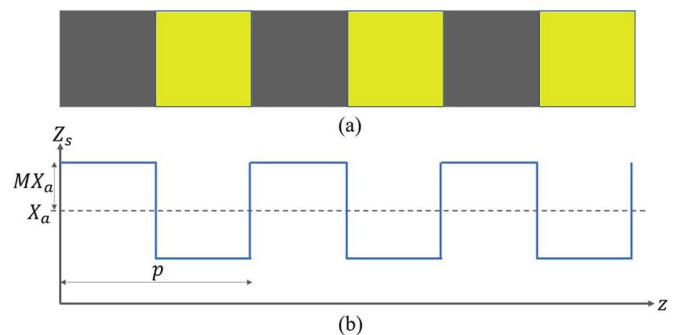

FIGURE 4. (a) One-dimensional equivalent of checkerboard surfaces, which are comprised of Artificial Magnetic Conductors (AMCs), shown in grey, and PECs, shown in lime, that have reflection phases of 0° and 180°, respectively. (b) A square-wave surface-impedance modulation function, where the half-periods are designed to have a reflection phase difference near 180° in order to mimic a checkerboard surface.

them more attractive than existing solutions. It should also be noted that LWAs can be employed irrespective of the car's bumper being flat or cylindrically curved [5].

A metasurface LWA flush-mounted on a car is illustrated in Fig. 3a. The RCS of automotive antennas is reduced to mitigate the destructive interference created by the standing waves from the multiple reflections between the antenna and the bumper [18], or the target (another car), as demonstrated in Fig. 3b. The destructive interference can hinder the detection and imaging of targets.

Square-wave modulation is used to excite leaky-wave modes in the metasurface and simultaneously mimic checkerboard surfaces to achieve RCS reduction, as illustrated in Fig. 4. The surface-impedance modulation function is expressed using a signum (sign) function, which represents square-wave modulation, as

$$Z_s(z) = jX_a\left\{1 + M\mathrm{sgn}\left[\cos\left(\frac{2\pi z}{p}\right)\right]\right\} \qquad (1)$$

where X_a is the average surface reactance, M is the modulation index and p is the modulation period. The modulation

period determines the elevation angle of the fan beam, while the average surface reactance and the modulation index control the gain and beamwidth. The square-wave modulation is realized by arranging metallic strips on a dielectric-covered ground plane; the gaps between the strips control the surface-reactance profile. This class of novel metasurfaces meets two design constraints: formation of a fan beam in the desired direction and low RCS under normal incidence. The impact of the modulation parameters on both the leaky-wave behavior and RCS reduction is analyzed to design low-RCS metasurface LWAs. The Floquet modes, pertaining to each Fourier harmonic with a significant amplitude coefficient, are examined and summed up vectorially to determine the radiation from the square-wave modulated surface. The low-RCS behavior is achieved by designing the metasurface with a reflection phase difference near 180° between two consecutive half-periods of the square-wave modulation. The incident energy is scattered away from the specular direction based on the generalized Snell's law of reflection.

The main contributions of this paper are as follows.

- A low-RCS antenna is realized without increasing the overall physical area or thickness of the radiating structure.
- An analytical model is developed to characterize the radiation properties of the square-wave modulated LWAs.
- The bistatic RCS pattern under normal incidence is predicted using an analytical expression that combines array theory and physical optics.
- The impact of each modulation parameter, such as the modulation period, average surface reactance, and modulation index on both radiation and RCS performances, is modeled and analyzed.
- A guideline for the range of reflection phase difference needed to achieve a 10-dB RCS reduction, relative to conventional sinusoidally-modulated LWAs, is recommended.
- The trade-off between RCS reduction and the sidelobe level is justified.

II. LWA THEORY

Conventional metasurface leaky-wave antennas are designed by modulating the surface impedance with a sinusoidal function given by [5], [7]

$$Z_{s1}(z) = jX_a\left\{1 + M\cos\left(\frac{2\pi z}{p}\right)\right\} \quad (2)$$

where X_a, M, and p are as defined in (1). When an LWA is sinusoidally impedance modulated with (2), the fundamental Floquet mode ($n = 0$) is a slow surface-wave mode. However, the $n = -1$ Floquet mode, and a few higher-order modes, are designed to be fast leaky-wave modes. In order to be a leaky-wave mode, the period p of the nth Floquet
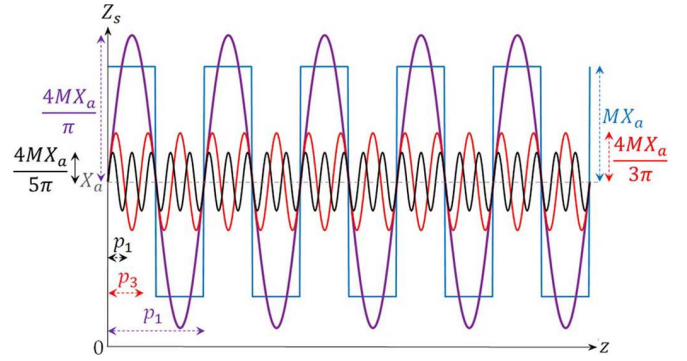

FIGURE 5. The square-wave surface-impedance modulation function (blue) and it's first three Fourier harmonics. The fundamental harmonic is shown in green, the third and the fifth harmonics are shown in red and black, respectively.

mode should satisfy the condition

$$\frac{|n|}{\sqrt{1 + \left(\frac{X_a}{\eta}\right)^2} + 1} \leq \frac{p}{\lambda} \leq \frac{|n|}{\sqrt{1 + \left(\frac{X_a}{\eta}\right)^2} - 1} \quad (3)$$

Each radiating leaky-wave mode forms a fan beam. Typically, the $n = -1$ Floquet mode forms the main lobe and the other Floquet modes contribute to the sidelobes.

The proposed LWAs are modulated with a square wave, as described in (1). Using Fourier series, the square-wave surface-impedance modulation function along the z-direction can be expressed as a sum of sinusoids and represented by

$$Z_s(z) = jX_a\left\{1 + M\left(\frac{4}{\pi}\right)\sum_{q=1,3,5,...}^{\infty}\frac{1}{q}\sin\left(\frac{2q\pi z}{p}\right)\right\} \quad (4)$$

where M denotes the modulation index, while q is used to index the Fourier harmonics. Equation (4) can be rewritten as

$$Z_s(z) = jX_a\left\{1 + \sum_{q=1,3,5,...}^{\infty}\left(\frac{4}{\pi}\right)M_q\sin\left(\frac{2\pi z}{p_q}\right)\right\} \quad (5)$$

where $p_q = p/q$ is the period and $M_q = M/q$ is the modulation index corresponding to the qth Fourier harmonic. A square wave has only odd Fourier harmonics and the period of the qth harmonic is shorter than that of the fundamental harmonic by a factor of $1/q$, as illustrated in Fig. 5.

When the surface impedance is modulated as a superposition of multiple sinusoids, multiple beams are formed corresponding to the sinusoids whose periodicity satisfies (3). The angular direction and gain of each beam are determined by the period and the modulation index, respectively, of the corresponding sinusoid [12], [31]. In a square-wave modulated LWA, for each Fourier harmonic expressed in (5), the fast leaky-wave modes radiate. The elevation angle of the fan-beam formed by the qth Fourier harmonic is expressed by

$$\theta_q = \sin^{-1}\left(\sqrt{1 + \left(\frac{X_a}{\eta}\right)^2} + \frac{2n\pi}{kp_q}\right) \quad (6)$$

where k is the free-space phase constant. The gain of the beam depends on the attenuation constant α_q of the qth

Fourier harmonic, which in turn is a function of M_q, X_a, and p_q corresponding to the Fourier harmonic. The attenuation constant corresponds to radiation, and it has to be non-zero for the Floquet mode to radiate. Hence, the gain increases with the attenuation constant up to a threshold value. However, when the attenuation constant is too large that the propagating leaky waves attenuate before utilizing the full aperture, the gain decreases. In this work, the goal is to increase the gain pertaining to the fundamental Fourier harmonic, while decreasing the gain of the higher-order Fourier harmonics; this should be achieved along with a low RCS. The attenuation/leakage constant α_q and the phase constant β_q can be determined by solving for the roots of the following continued fraction, as described in [2]

$$1 - \frac{j}{X_a}\sqrt{1 - \left(\frac{\kappa}{k_0}\right)^2}$$
$$= \cfrac{M^2/4}{1 - \frac{j}{X_a}\sqrt{1 - \left(\frac{\kappa}{k_0} + \frac{2\pi}{k_0 p}\right)^2} - \cfrac{M^2/4}{1 - \frac{j}{X_a}\sqrt{1 - \left(\frac{\kappa}{k_0} + \frac{4\pi}{k_0 p}\right)^2} - \cdots}}$$
$$+ \cfrac{M^2/4}{1 - \frac{j}{X_a}\sqrt{1 - \left(\frac{\kappa}{k_0} - \frac{2\pi}{k_0 p}\right)^2} - \cfrac{M^2/4}{1 - \frac{j}{X_a}\sqrt{1 - \left(\frac{\kappa}{k_0} - \frac{4\pi}{k_0 p}\right)^2} - \cdots}}$$
(7)

where $\kappa = \beta - j\alpha$ is the propagation constant of the fundamental Floquet mode.

The dispersion diagram (k_0 vs β), for a given average surface reactance X_a and modulation index M, can be plotted using (7). For smaller values of M, a simplified solution to the continued fraction is proposed in [2], [7]. As an illustration, the dispersion diagram corresponding to $X_a = 226.2\ \Omega$ and $M = 0.4$ is displayed in Fig. 6. The bandgaps, which correspond to the frequencies with no surface/leaky-wave propagation, are highlighted with the dashed red circles and they occur for modulated surface impedances when βp is a multiple of π. The slope of the curve decreases as X_a increases. The bandgap does not exist for the case of no modulation and it widens as M increases [2]. The value of the fundamental period p_1 of the square wave is determined by the desired direction of the fan beam θ_1. Based on the choice of θ_1, and hence p_1, the $k_0 p_3$ corresponding to the 3rd Fourier harmonic might fall in the bandgap region, resulting in no radiation. This means that the sidelobe that is formed by the third Fourier harmonic can be mitigated.

In the proposed case of square-wave modulation, the average surface reactance is constant for all Fourier harmonics. However, the variation in the attenuation and the phase constants, with respect to the modulation index, is different for each Fourier harmonic due to their unequal periodicities. The variation of the attenuation and the phase constants of the fundamental Fourier harmonic, with respect to the modulation index M of the square-wave modulation, for $X_a = 226.2\ \Omega$ are plotted in Figs. 7 and 8. It should be
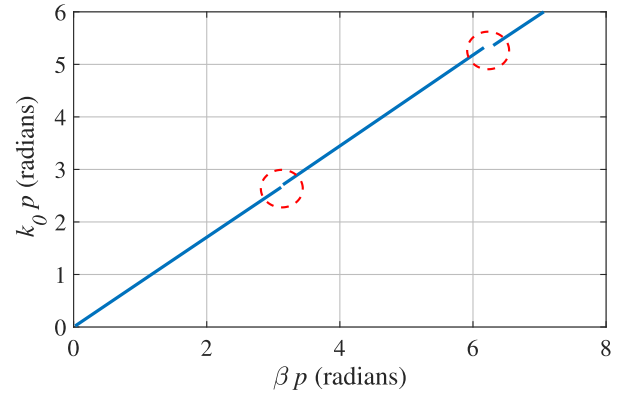

FIGURE 6. The dispersion diagram of a sinusoidally-modulated LWA, with $X_a = 226.2\ \Omega$ and $M = 0.4$. The bandgaps are circled in red. The phase constant, β of each Fourier harmonic can be obtained from this plot using the corresponding period, p_q.
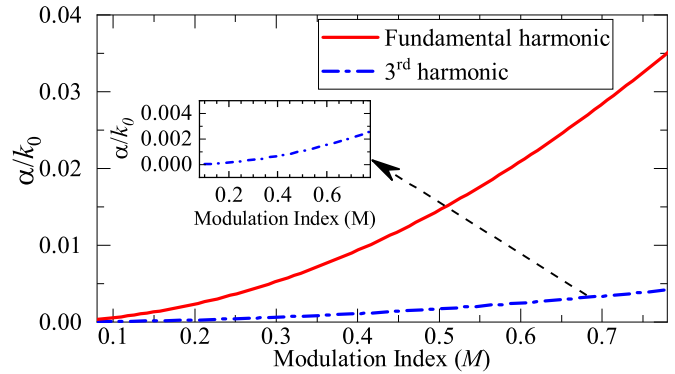

FIGURE 7. The variation of the attenuation constants of the fundamental and the third Fourier harmonics with the modulation index of the square-wave modulation. The period of this harmonic p_1 is 1.5λ, the frequency of operation is 15 GHz and $X_a = 226.2\ \Omega$. As the range of the attenuation constant pertaining to the third Fourier harmonic is smaller compared to the fundamental harmonic, the variation is also shown using an inset plot.

noted that the modulation index of the fundamental Fourier harmonic is $4/\pi$ times that of the square-wave modulation, while the modulation index of the 3rd Fourier harmonic is $4/(3\pi)$ times that of the square-wave modulation. The period of the fundamental Fourier harmonic is 1.5λ at the operation frequency of 15 GHz; λ corresponds to the free-space wavelength. This leaky-wave antenna forms a fan beam along $30°$ from broadside, as it will be demonstrated in the sections that follow.

The far-zone fields radiated by the square-wave modulated checkerboard LWA can be obtained by employing physical optics on the aperture fields, as detailed in [32], [38]. Using the Floquet theorem, the aperture magnetic fields can be expressed as [2]

$$\mathbf{H_a}(z) = \hat{\mathbf{a}}_y\, e^{-j\kappa z} \sum_{n=-\infty}^{\infty} \frac{I_n}{\sqrt{2\pi}} e^{-j(2n\pi/a)z} \tag{8}$$

The aperture fields can be determined by the surface impedance boundary condition

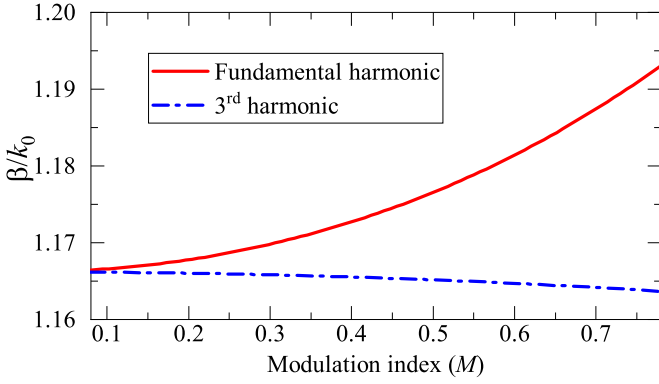$$\mathbf{E_a} = Z_s(\hat{\mathbf{n}} \times \mathbf{H_a}) \tag{9}$$

FIGURE 8. The variation of the phase constants of the fundamental and the third Fourier harmonics with the modulation index of the square-wave modulation. The period of this harmonic p_1 is 1.5λ, the frequency of operation is 15 GHz and $X_a = 226.2$ Ω.
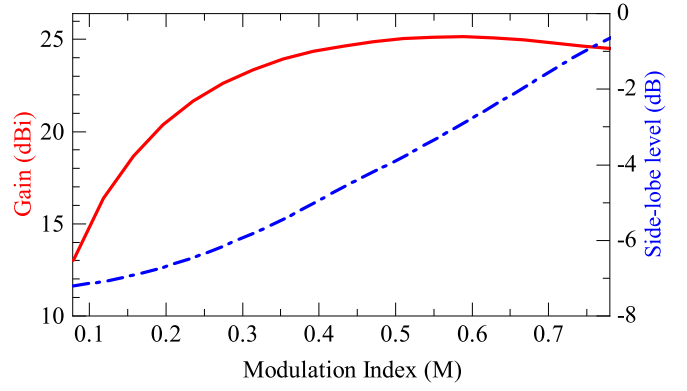

FIGURE 9. The variation of the gain and sidelobe level with the modulation index of a square-wave modulated LWA with $p = 1.5λ$, $X_a = 226.2$ Ω, at a frequency of 15 GHz.

Considering only the fundamental and the third Fourier harmonics of the square wave modulation, their respective harmonic aperture fields are expressed as

$$\mathbf{E_{a-1^{st}}}(z) = \hat{\mathbf{a}}_z \, jX_a \left[1 + M\left(\frac{4}{\pi}\right) \sin\left(\frac{2\pi z}{p}\right) \right]$$
$$\times \; e^{-(\alpha+j\beta)z} \sum_{n=-\infty}^{\infty} \frac{I_n}{\sqrt{2\pi}} e^{-j(2n\pi/p)z} \quad (10)$$

$$\mathbf{E_{a-3^{rd}}}(z) = \hat{\mathbf{a}}_z \, jX_a \left[1 + M\left(\frac{4}{3\pi}\right) \sin\left(\frac{6\pi z}{p}\right) \right]$$
$$\times \; e^{-(\alpha_1+j\beta_1)z} \sum_{n=-\infty}^{\infty} \frac{I'_n}{\sqrt{2\pi}} e^{-j(6n\pi/p)z} \quad (11)$$

$$\mathbf{E_{a-total}}(z) = \mathbf{E_{a-1^{st}}}(z) + \mathbf{E_{a-3^{rd}}}(z) \quad (12)$$

where $\kappa_1 = \beta_1 - j\alpha_1$ is the propagation constant of the fundamental surface-wave mode ($n = 0$ Floquet mode) of the 3rd Fourier harmonic, I_n and I'_n are the magnitudes of the mode currents of the nth Floquet mode for the fundamental and the 3rd Fourier harmonics, respectively. The propagation constants can be determined using (7), while κ_1 can be obtained from (7) by replacing M with $M1 = M/3$ and p with $p1 = p/3$. The mode currents can be determined using [2]

$$\frac{-I_{n+1}}{I_n} = \frac{2}{M}\left(1 - \frac{j}{X_a}\sqrt{1 - \left(\frac{\kappa}{k_0} + \frac{2\pi n}{k_0 p}\right)^2} \right)$$
$$- \frac{1}{\frac{2}{M}\left(1 - \frac{j}{X_a}\sqrt{1 - \left(\frac{\kappa}{k_0} + \frac{2\pi (n-1)}{k_0 p}\right)^2} \right) - \frac{1}{\dots}} \quad (13)$$

$$\frac{-I'_{n+1}}{I'_n} = \frac{6}{M}\left(1 - \frac{j}{X_a}\sqrt{1 - \left(\frac{\kappa}{k_0} + \frac{6\pi n}{k_0 p}\right)^2} \right)$$
$$- \frac{1}{\frac{6}{M}\left(1 - \frac{j}{X_a}\sqrt{1 - \left(\frac{\kappa}{k_0} + \frac{6\pi (n-1)}{k_0 p}\right)^2} \right) - \frac{1}{\dots}} \quad (14)$$

Rewriting (10) and (11) as a sum of infinite Floquet modes

$$\mathbf{E_{a-1^{st}}}(z) = \hat{\mathbf{a}}_z \, j\frac{X_a}{\sqrt{2\pi}} \sum_{n=-\infty}^{\infty} \left(I_n - \frac{M}{2j}I_{n-1} + \frac{M}{2j}I_{n+1} \right)$$
$$\times \; e^{-(\alpha+j\beta+j2\pi n/p)z} \quad (15)$$

$$\mathbf{E_{a-3^{rd}}}(z) = \hat{\mathbf{a}}_z \, j\frac{X_a}{\sqrt{2\pi}} \sum_{n=-\infty}^{\infty} \left(I'_n - \frac{M}{6j}I'_{n-1} + \frac{M}{6j}I'_{n+1} \right)$$
$$\times \; e^{-(\alpha_1+j\beta_1+j6\pi n/p)z} \quad (16)$$

the far-zone fields can be computed by employing physical optics on the fast-wave modes. The co-polarized radiated far-zone fields can be represented by

$$\mathbf{E} = \hat{\mathbf{a}}_\theta \left\{ jkw_1 \frac{X_a \sin\theta \cos\phi}{4\pi\sqrt{2\pi}} \left[\frac{\sin(k(w_1/2)\sin\theta \sin\phi)}{k(w_1/2)\sin\theta \sin\phi} \right] \right\}$$
$$\times \left\{ \left[\sum_{n=-\infty}^{\infty} \left(I_n - \frac{M}{2j}I_{n-1} + \frac{M}{2j}I_{n+1} \right) \right.\right.$$
$$\times \left. \left(\frac{1 - e^{-j(\kappa+(2n\pi/p)-k\cos\theta)l_1}}{j(\kappa + +(2n\pi/p) - k\cos\theta)l_1} \right) \right]$$
$$+ \left[\sum_{n=-\infty}^{\infty} \left(I'_n - \frac{M}{6j}I'_{n-1} + \frac{M}{6j}I'_{n+1} \right) \right.$$
$$\times \left.\left. \left(\frac{1 - e^{-j(\kappa_1++(6n\pi/p)-k\cos\theta)l_1}}{j(\kappa_1 + +(6n\pi/p) - k\cos\theta)l_1} \right) \right] \right\} \quad (17)$$

where w_1 and l_1 are the width and length, respectively, of the antenna's aperture. These far-zone fields only include the first and third Fourier harmonics. However, if the higher-order harmonics satisfy the radiation condition of (3), the expression for the far-zone fields in (17) can be extended by including the Floquet modes corresponding to those Fourier harmonics.

The gain and sidelobe level of a square-wave-modulated LWA is shown in Fig. 9. The antenna is 12λ long, 1.5λ wide, with an average surface reactance of 226.2 Ω, a periodicity of 1.5λ, and operated at 15 GHz. As a function of the modulation index, the gain monotonically increases, reaches a maximum, and then decreases, as the leaky waves begin

to decay before utilizing the full aperture. The sidelobe corresponding to the third Fourier harmonic increases with M, as the modulation index of that harmonic is only $1/3^{rd}$ of that of the fundamental harmonic.

The $n = -1$ Floquet mode is a propagating surface-wave mode in the absence of modulation and it becomes a leaky-wave mode due to the periodic impedance modulation. As illustrated in Fig. 7, the attenuation/leakage constant increases with the modulation index, and hence the gain increases initially. However, with a large modulation index, the leaky waves do not utilize the complete aperture and hence the gain decreases, as observed in Fig. 9.

The sidelobes are influenced by the 3rd Fourier harmonic and possibly by the $n = -2$ Floquet mode pertaining to each Fourier harmonic. It can be shown from (13) and (14) that, for smaller values of M, the largest sidelobe pertains to the $n = -1$ Floquet mode of the 3rd Fourier harmonic. As the modulation index increases, (I_{-2}/I_{-1}) increases more drastically than (I'_{-1}/I_{-1}). Hence, for large modulation indices, the major sidelobe is formed by the $n = -2$ Floquet mode of the fundamental Fourier harmonic.

The modulation index corresponding to the 3rd Fourier harmonic M_3 is $1/3^{rd}$ of that of the fundamental harmonic M_1. Based on Fig. 7, the attenuation constant of the 3rd Fourier harmonic is much smaller than that of the fundamental harmonic. Similarly, the radiation from the $n = -2$ Floquet mode of the fundamental Fourier harmonic drastically increases with M. Hence, the gain corresponding to the sidelobe increases with M, while that of the main lobe decreases. Thus, it is important to optimize the parameter M to maximize gain and minimize the sidelobe level.

III. RCS REDUCTION OF METASURFACE LEAKY-WAVE ANTENNAS

Metasurface LWAs can be realized by modulating the surface impedance with a periodic function: a sinusoidal function, as shown in (2) in the case of conventional metasurface LWAs or a square-wave modulation as expressed by (1). The periodicity in the structure scatters the normally-incident plane waves into different directions, including the specular direction. In this paper, for modulated metasurfaces with an inductive surface-reactance profile, the RCS under normally-incident TM^x plane waves in which the electric field is transverse to the strips is considered; x is normal to the LWA's aperture. For TE^x polarized incident waves, RCS reduction can be achieved by employing modulated metasurfaces with a capacitive surface-reactance profile.

A. RCS OF SINUSOIDALLY-MODULATED METASURFACES

The scattering of normally-incident plane waves by periodic metasurface LWAs can be interpreted using grating theory. It can be shown using the grating equation that the minimum periodicity p required to excite the $m = \pm 1$ diffraction modes is one wavelength. This sets a minimum bound on
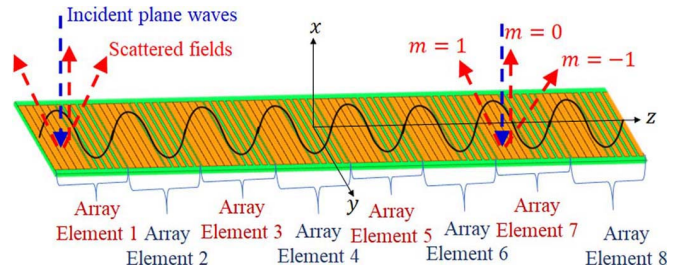

FIGURE 10. The bistatic RCS pattern of a sinusoidally-modulated LWA can be obtained using array theory. Each period of the sinusoidal modulation is considered as an array element. The direction of scattered beams formed by the diffraction modes $m = 0, \pm 1$ can also be determined using grating theory.

the period of modulation, for a given frequency of operation, to scatter the normally-incident plane waves into other angular directions, besides the specular. The directions of the scattered beams can be determined using the grating equation [34]

$$\theta_m = \sin^{-1}\left(\frac{m\lambda}{p}\right) \qquad (18)$$

where $m = 0, \pm 1, \pm 2, \ldots$ indexes the diffraction modes pertaining to grating diffraction.

The bistatic RCS pattern of a sinusoidally-modulated metasurface LWA can be obtained using array theory, as illustrated in Fig. 10 [33]. Each period of the sinusoidal modulation can be considered as an array element and the separation between the array elements, which can be defined as the distance between the center of an array element and that of a subsequent one, is equal to the periodicity p of the sinusoidal modulation. The array factor AF is expressed as [32]

$$AF(\theta) = \sum_{n=1}^{N} e^{j(n-1)(kp\cos\theta + \beta_p)} \qquad (19)$$

where N is the number of periods of the sinusoidal modulation and β_p is the progressive reflection phase difference between the array elements. The progressive reflection phase shift in a conventional sinusoidally-modulated metasurface is zero. The AF predicts the positions of the lobes in the RCS pattern, while the complete bistatic RCS pattern can be obtained as a product of the array factor and the element factor EF.

It is possible to determine the element factor by modeling each period as a sub-array, where the sub-array elements are unit cells comprised of a strip and gaps on either side [33]. However, this method is inaccurate, particularly when the unit cell size becomes very small compared to the wavelength. For a more accurate model, the normalized element factor is determined by employing physical optics on one period of the sinusoidal modulation. Employing physical optics to determine the bistatic RCS of metasurfaces results in an accurate pattern at and near the specular direction [37].

Each period of the sinusoidal modulation comprises of metallic strips separated by varying gap sizes; the reflection
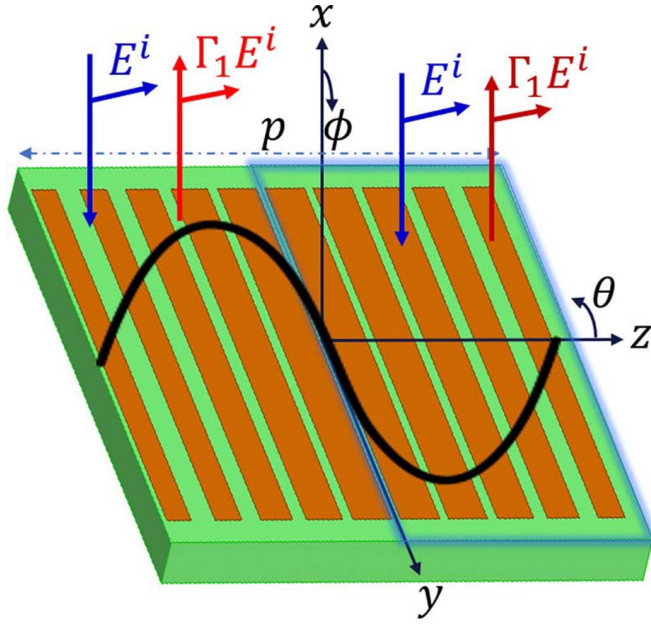
FIGURE 11. The element factor is determined using physical optics on one period of the sinusoid. The reflection phase of each half-period, highlighted in blue, can be approximated to that of the gap corresponding to the X_a.
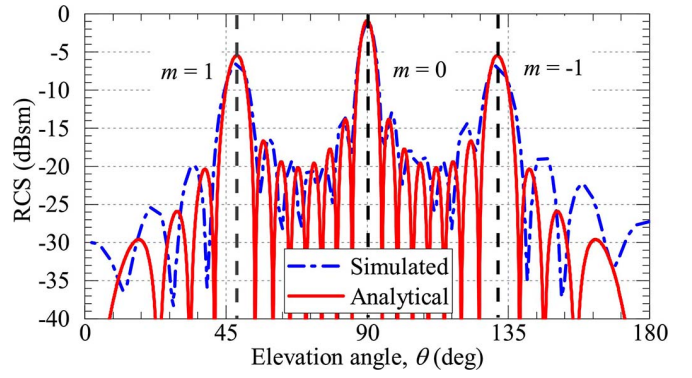

FIGURE 12. Comparison between the analytically predicted bistatic RCS of the sinusoidally-modulated metasurface and full-wave EM simulations. The angle of incidence is $\theta_i = 90°$ and the incident energy is coupled to $m = 0, \pm1$ diffraction modes.

phase also varies sinusoidally within the array element. The overall reflection phase of the inhomogeneous array element can be approximated by splitting the sinusoidal period into two half-periods. A half-period is an optimal division as it is not too large to increase the approximation error, while its size is still comparable to the wavelength of the incident plane waves. The average value of the sinusoidally-varying reflection phase of one half-period is equal to the average value of the full period. Hence, the reflection phase of each half-period can be approximated, as illustrated in Fig. 11. The amplitude of the reflection coefficient is taken as unity when determining the normalized element factor. To denormalize the element factor, the fraction of the energy that is reflected along the specular direction needs to be determined. When the modulation period is greater than a wavelength, the energy from the impinging plane waves is coupled to more than one diffraction mode.

Floquet-mode simulations can be used to determine the fraction of energy coupled to each diffraction mode [16]. In a Floquet-mode simulation, periodic boundary conditions are applied to the array element, which corresponds to one period of the sinusoidal modulation. The surface is excited using a Floquet port, with its mode corresponding to TM^x polarization. The energy coupled to each diffraction mode can be determined from the corresponding S-parameters.

Using physical optics [38], the normalized element factor can be expressed as

$$EF_n(\theta) = \left[\frac{\sin(0.5kp\cos\theta)}{0.5kp\cos\theta} - j\frac{\sin^2(0.25kp\cos\theta)}{0.25kp\cos\theta} \right] \times [1 + \Gamma_1 - \sin\theta(1 - \Gamma_1)] \quad (20)$$

The complex reflection coefficient Γ_1 of the half-period can be expressed, using either Floquet-mode simulations or the LC model for high-impedance surfaces, as [35]

$$Z = \frac{j2\pi^2 f\mu h}{\pi - k^2h(a - g_a)(\epsilon_r + 1)\cosh^{-1}(a/g_a)} \quad (21)$$

where a is the size of the unit cell, h is the thickness of the substrate and ϵ_r is the dielectric constant of the substrate, as detailed in Fig. 11. The magnitude of Γ_1 is taken as unity to determine the normalized element factor. The reflection phase is represented by

$$\Gamma_1 = \frac{Z - \eta}{Z + \eta} \quad (22)$$

This analytical model is used to predict the bistatic RCS of a sinusoidally-modulated metasurface which has a periodicity of 1.5λ, eight modulation periods, and a 1.524 mm thick substrate, with a width of 1.5λ and a dielectric constant of 3. Using the Floquet-mode simulations for this geometry, the amplitude of the element factor is 0.74. The comparison between the analytical model and full-wave EM simulations in HFSS is shown in Fig. 12. It is observed that there is an excellent agreement between the analytical model and the simulations, particularly near the specular direction. The slight disagreement for angles far away from the specular direction is a limitation of physical optics.

B. RCS REDUCTION TECHNIQUES
The RCS of metasurface LWAs can be reduced by modulating the surface impedance with a square wave, which mimics checkerboard surfaces. When plane waves are normally incident on a checkerboard of alternating surfaces that have a 180° reflection phase difference between each other, a null is formed along the specular direction [30]. Commonly, one of the surfaces is a PEC and the other one is an AMC that mimics a PMC at a particular frequency.

Checkerboard surfaces are conventionally two dimensional. For one-dimensional equivalents of checkerboard surfaces shown in Fig. 4a, the RCS variation can be detailed

using the array theory-based model of Section III-A. While the array factor is similar to that defined in (19), the element factor can be expressed, using physical optics, as

$$EF_n(\theta) = \left[\frac{\sin(0.5kp\cos\theta)}{0.5kp\cos\theta} - j\frac{\sin^2(0.25kp\cos\theta)}{0.25kp\cos\theta} \right]$$
$$\times [1 + \Gamma_1 - \sin\theta(1 - \Gamma_1)]$$
$$+ \left[\frac{\sin(0.5kp\cos\theta)}{0.5kp\cos\theta} + j\frac{\sin^2(0.25kp\cos\theta)}{0.25kp\cos\theta} \right]$$
$$\times [1 + \Gamma_2 - \sin\theta(1 - \Gamma_2)] \quad (23)$$

where Γ_1 and $\Gamma_2 = \Gamma_1 e^{j\beta_{p2}}$ are the complex reflection coefficients of the two half-periods of the square-wave modulation. The element factor reduces to zero along the specular direction ($\theta = 90°$) when the metasurfaces in a checkerboard pattern are 180° out of phase (that is, $\beta_{p2} = 180°$).

Based on the generalized Snell's law of reflection, the sudden phase shift of 180°, which occurs periodically with a period of $p/2$, changes the specular direction to

$$\theta_s = \cos^{-1}\left(\frac{\lambda}{2\pi}\frac{d\Phi}{dz} \right) = \cos^{-1}\left(\frac{\pm\lambda}{p} \right) \quad (24)$$

The angles represented by (24) coincide with the scattered beams formed by grating diffraction determined using (18). Hence, the main beams of the bistatic RCS patterns are constituted only by the beams corresponding to the $m = \pm 1$ diffraction modes.

In conventional checkerboard surfaces, to achieve a 10-dB RCS reduction relative to a PEC, the reflection phase difference should be $180° \pm 37°$ [30]. However, this condition does not apply to this work, as the reference is a sinusoidally-modulated LWA. This paper focuses on square-wave-modulated metasurfaces, which also include a one-dimensional equivalent of conventional PEC-PMC checkerboard. It can be shown using grating theory that the periodicity should be greater than one wavelength to scatter the incident plane waves into multiple directions. For instance, the bistatic RCS pattern of a PEC - PMC checkerboard under normal incidence, whose periodicity is less than a wavelength, is shown in Fig. 13. The periodicity of the checkerboard surface is $\lambda/2$ and the size of the PEC and PMC cells are equal. As the periodicity is small, the energy from the impinging plane waves is coupled to only the $m = 0$ diffraction mode, which is along the specular direction, in spite of the 180° reflection phase difference between the cells. On the other hand, a larger periodicity ($p \geq 2\lambda$) couples the impinging energy to five or more diffraction modes.

The reflection phase difference needed for RCS reduction can be obtained by varying the gap size used in each half-period. The reflection phase for a given gap size can be obtained from (21) and (22) or using full-wave EM simulations. For a metasurface unit cell of size 0.15λ, with a substrate of dielectric constant 3 and thickness 0.076λ, the reflection phase for different gap sizes is plotted in Fig. 14.

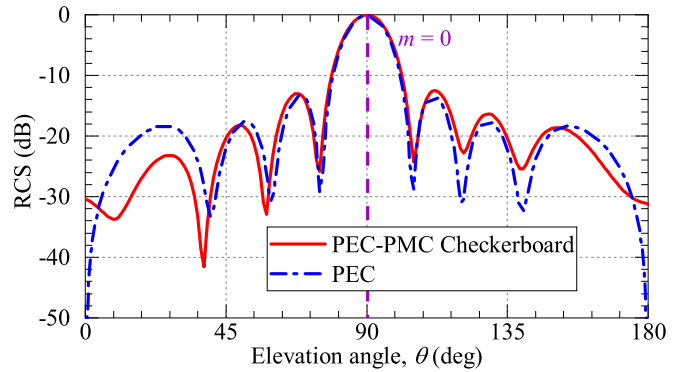**FIGURE 13.** The bistatic RCS pattern of a 1-D PEC-PMC checkerboard whose periodicity is λ/2 is compared to that of a PEC of the same geometry. The angle of incidence is $\theta_i = 90°$, and the energy from the incident waves is coupled only to the $m = 0$ diffraction mode, in spite of the 180° reflection phase difference.
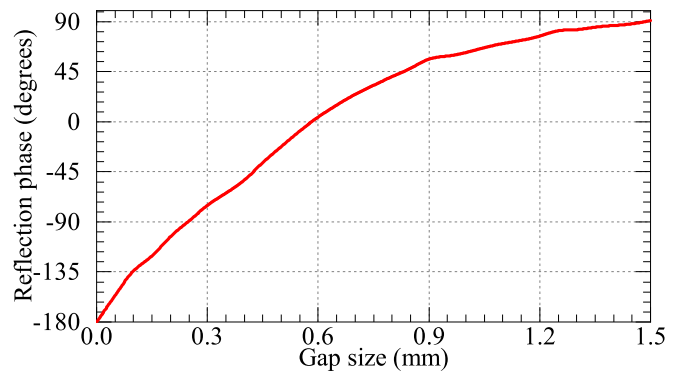

FIGURE 14. Variation of the reflection phase with respect to the gap size at 15 GHz for a unit cell of 0.15λ with a substrate of dielectric constant 3 and thickness 0.076λ.

It is observed from Fig. 14 that the reflection phase varies rapidly for smaller gap sizes and the variation flattens as the gaps become larger. Hence, the pair of gap sizes that correspond to the two half-periods of the square-wave modulation should be selected judiciously to obtain a 180° progressive reflection phase difference. Between the pair of the selected gap sizes, if the smallest value (that usually corresponding to the first half-period of the square-wave modulation) is not sufficiently small, then due to the slope of the curve in Fig. 14, the needed 180° reflection phase difference cannot be obtained. For instance, if the smallest gap size is 0.4 mm, the corresponding reflection phase from Fig. 14 is $-45°$; hence, the other half-period should have a reflection phase of 135°. However, this cannot be obtained as it is outside the feasible range of reflection phases for this geometry. Even if the smallest gap size is as small as 0.1 mm, the other gap size needs to be as large as 0.9 mm, which would use about 53% of the range of gap sizes included in Fig. 14. Hence, the main conditions to obtain a 180° reflection phase shift are:

1) The gap size corresponding to one half-period needs to be very small.
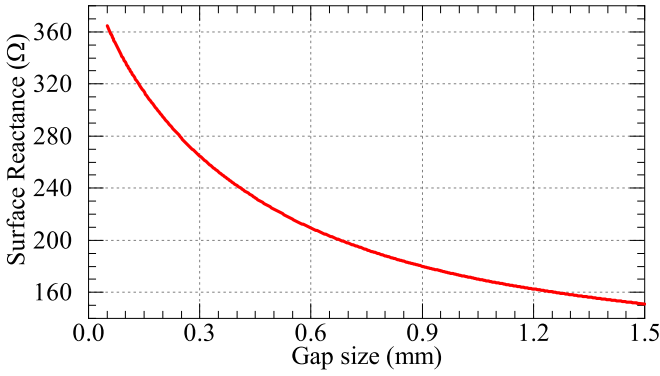2) The other half-period should have a large gap size, thus resulting in a large modulation index.

FIGURE 15. Variation of the surface reactance with respect to the gap size at 15 GHz for a unit cell of 0.15λ with a substrate of dielectric constant 3 and thickness 0.076λ.
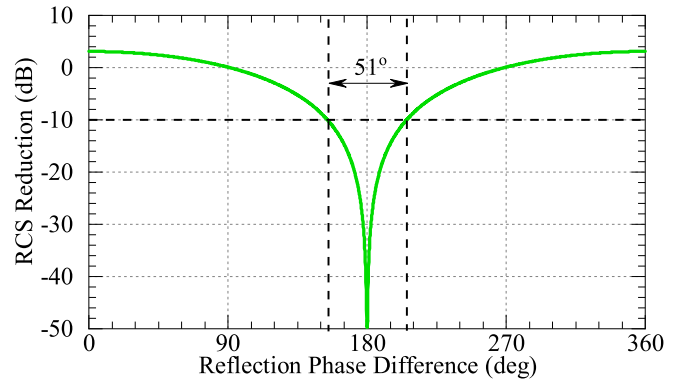

FIGURE 16. Variation of the RCS reduction with respect to the reflection phase difference between the two half-periods at 15 GHz for a unit cell of 0.15λ with a substrate of dielectric constant 3 and thickness 0.076λ.

The choice of the gap sizes sets the values of the average surface reactance X_a and the modulation index M. It should be noted that X_a and M not only impact the radiation characteristics of the LWA, but also the RCS. The relationship between the gap sizes and the modulation parameters, such as the average surface reactance and the modulation index, can be inferred by plotting the variation of the surface reactance with respect to the gap size, as illustrated in Fig. 15. The geometry of the unit cell used in Fig. 15 is the same as that in Fig. 14. The surface-reactance variation can be obtained using the Transverse Resonance Method (TRM), as detailed in [36].

The surface reactance, shown in Fig. 15 varies rapidly for smaller gap sizes while the variation flattens for larger values; this is similar to the behavior of the reflection phase with respect to the gap sizes displayed in Fig. 14. Consequently, when the gap size of one half-period is very small (for instance, below 0.2 mm), it corresponds to a large surface reactance. Moreover, the surface-reactance variation is drastic when the gap size of the other half-period is large. These conditions, which are needed to obtain a 180° reflection phase shift between the two half-periods, result in a large surface-reactance variation between the two half-periods, thus implying a higher average surface reactance X_a and a larger modulation index M. Nevertheless, a reflection phase difference of 180° is required to create a null along the specular direction. When the application can accept a finite but low RCS along the specular direction, a reflection phase difference that is slightly smaller than 180° can be used. This relaxes the condition on X_a and M and, hence, improves the radiation performance of the antenna.

IV. DESIGN OF METASURFACE LWAS WITH LOW RCS
The design of one-dimensionally periodic modulated metasurface LWAs involves the estimation of X_a, M, and p to form a fan beam in the desired direction. While X_a and p determine the direction of the fan beam, M controls the gain, beamwidth, and the sidelobe level. However, these modulation parameters also control the RCS of the antenna. The

designs of low-RCS LWAs need to satisfy the requirements pertaining to both radiation and scattering. While the radiation requirements necessitate a specific set of values for the modulation parameters, the scattering requirements might require a different set of values. Hence, there is a trade-off between the radiation performance and RCS reduction. For instance, while a large modulation index is needed for a greater RCS reduction, it results in a higher sidelobe level, as illustrated in Fig. 9. In this section, a low-RCS leaky-wave antenna is designed to operate at 15 GHz using the same geometry described in Section III-A.

A. AVERAGE SURFACE REACTANCE
In the design of LWAs, the average surface reactance is selected from the plot of surface reactance for different gap sizes, as shown in Fig. 15. Based on the realizable range of reactances, for the desired modulation index, a reasonable value of X_a is selected. To achieve low RCS, a reflection phase difference near 180° is needed. The RCS reduction with respect to a conventional sinusoidally-modulated LWA can be expressed as

$$\text{RCS reduction} = 10 \log \left[\frac{\left| EF_{\text{proposed}} \right|^2}{\left| EF_{\text{conventional}} \right|^2} \right] \quad (25)$$

where EF_{proposed} and $EF_{\text{conventional}}$ refer to the element factors of the proposed square-wave modulated LWAs and the conventional sinusoidally-modulated LWAs, respectively, and they are determined using (20) and (23).

Fig. 16 displays the level of RCS reduction achieved at 15 GHz by the square-wave-modulated metasurfaces, relative to the conventional sinusoidally-modulated metasurfaces, as a function of the relative reflection phase shift between the two half-periods. It is observed that a reflection phase difference of $180° \pm 25.5°$ is needed between the two half-periods of the square-wave modulation to achieve a 10-dB RCS reduction relative to a sinusoidally-modulated LWA. Hence, from Fig. 14, it is desired to have a smaller gap size corresponding to X_a; thus, a larger value of X_a. Nonetheless,
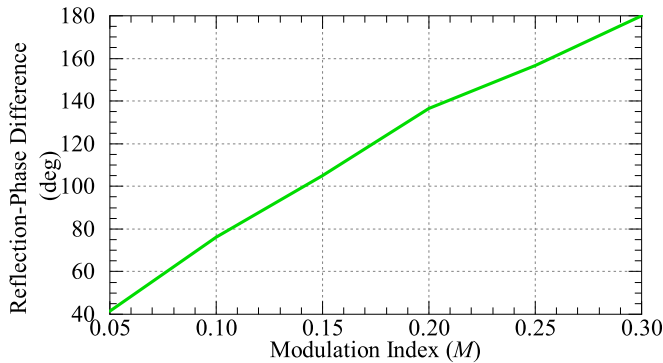
FIGURE 17. The reflection phase difference between the two half-periods as a function of the modulation index for $X_a = 226.2$ Ω at 15 GHz for a unit cell of 0.15λ with a substrate of dielectric constant 3 and thickness 0.076λ.

it can be derived from (6) that a larger value of X_a necessitates a smaller value of the periodicity p to form the beam in the desired direction. However, RCS reduction cannot be achieved if the period is less than one wavelength and a small period decreases the RCS-reduction bandwidth. Moreover, a smaller value of X_a demands a larger modulation index M to achieve the needed $180° \pm 25.5°$ reflection phase difference. Considering these constraints on the average surface reactance, an optimal value should be chosen based on the radiation and RCS requirements of the application. For the geometry considered in this paper, an optimal value of the average surface reactance would be $X_a = 226.2\Omega$, which corresponds to a gap size of $480\mu m$, as determined from Fig. 15.

B. MODULATION INDEX

The modulation index of a leaky-wave antenna is determined based on the choice of the average surface reactance, desired gain, beamwidth, and sidelobe level. A smaller non-zero modulation index is preferred, as a large M results in a lower gain and a larger sidelobe level, as illustrated in Fig. 9. The sidelobe level steeply increases with the modulation index for square-wave modulated LWAs; the value of M is set by X_a. For the value of the average surface reactance selected in the previous subsection, $X_a = 226.2\Omega$, an optimal value of M, for a high gain and a lower sidelobe level, would be about 0.2. The reflection phase difference between the two half-periods, as a function of the modulation index, for this geometry is plotted in Fig. 17. It is observed that a modulation index of 0.29 is needed to achieve a $180°$ reflection phase difference. Nevertheless, a modulation index of 0.25 would suffice to achieve a 10-dB RCS reduction. Increasing the modulation index from 0.2 to 0.29 increases the sidelobe level by 0.5 dB. It should be noted that the modulation index corresponding to the fundamental Fourier harmonic is greater by a factor of $(4/\pi)$ than that of the square-wave. Hence, increasing the modulation index of the square-wave modulation to achieve the reflection phase difference results in a larger increase of the modulation index pertaining to the radiating Floquet modes of the first and third Fourier harmonics.

C. MODULATION PERIOD

The period of the surface-impedance modulation function determines the angular direction of the radiated fan beam. To form a fan beam in the desired angular direction θ_d from the broadside, the modulation period is determined by [7]

$$p = \frac{2\pi}{k\sqrt{1 + (X_a/\eta)^2} - k\sin\theta_d} \tag{26}$$

With the considered geometry, the modulation period needed to form a beam at $30°$ from broadside is 1.5λ. For RCS reduction, the periodicity should be at least one-wavelength; this limits the scan-angle range of the antenna. Hence, the frequency scanning using the geometry used in this paper, with $X_a = 226.2$ Ω and $p = 1.5\lambda$, is limited to the forward quadrant, with the minimum scan angle of $9.5°$. The scan-angle range can be increased by decreasing the average surface reactance. However, a lower X_a value would force a larger modulation index to achieve the reflection phase difference needed for RCS reduction.

D. DESIGN GUIDELINES

The procedure to design low-RCS LWAs can be summarized as:

- Determine a sufficiently high average surface reactance from Fig. 14, based on the required RCS reduction.
- Verify that the modulation period, corresponding to the determined average surface reactance, is larger than one wavelength.
- Select the modulation index required for the desired level of RCS reduction from Fig. 17.
- Calculate the modulation period needed to form the fan beam in the desired direction using (26).
- Verify that the design satisfies the sidelobe level requirements using Fig. 9. The RCS requirements need to be relaxed to improve the sidelobe level.

V. RESULTS AND DISCUSSION

Based on the suggested guidelines, a low-RCS LWA was designed to form a fan beam at $30°$ from broadside at 15 GHz. The antenna was realized using metallic strips of width 1.5λ and eight modulation periods resulting in an overall length of 12λ. The design parameters of the antenna were the same as those specified in Section IV. A modulation index of 0.29 was used to achieve near a $180°$ reflection phase difference between the half-periods.

A prototype of the antenna, with the above-mentioned design parameters, was fabricated. The metallic pattern was masked on a Rogers 3003 substrate ($\varepsilon_r = 3$ and $\tan\delta = 0.0013$) and the gaps were chemically etched. The need to use a very small gap size (around 100-200 μm) for one half-period requires a high-resolution mask of the metallic pattern. As the reflection phase varies rapidly with gap sizes, particularly for the first half-period, the design is sensitive to fabrication errors.
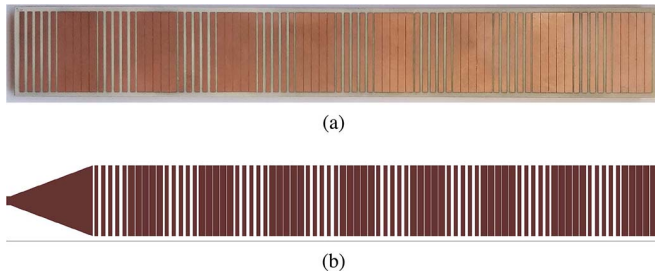
FIGURE 18. (a) The fabricated prototype used for RCS measurements. **(b)** The high-resolution artwork of the antenna, along with the matching network, used to fabricate the prototype for antenna measurements.
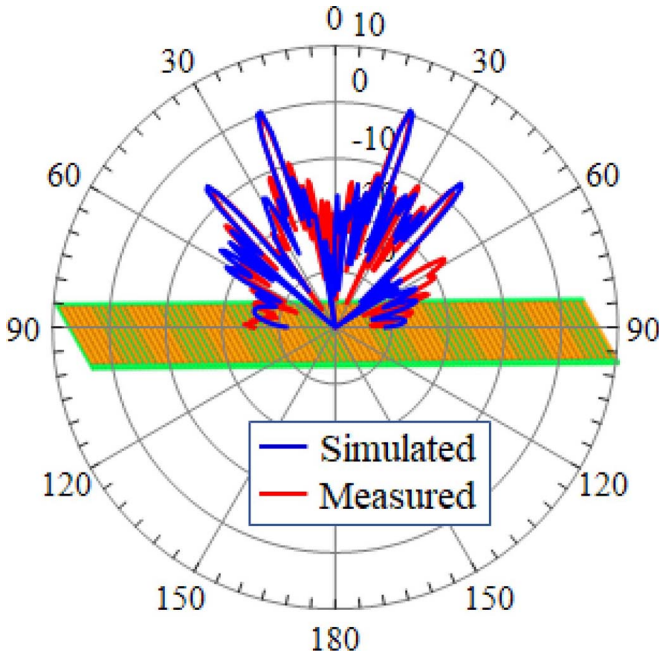

FIGURE 19. The comparison between the simulated and measured monostatic RCS patterns. An RCS reduction of about 20 dB is achieved relative to a sinusoidally-modulated LWA.

The antenna was fabricated with a tapered matching network, and it was excited from one end using a 50-Ω SMA cable. The antenna's radiation and the monostatic RCS patterns were measured. For RCS measurements, another metasurface with the same metallic pattern was fabricated without the matching network. As an alternative, the matching network and the SMA connector could have also been masked with an absorber while measuring the RCS of the antenna. The fabricated prototype without the matching network is shown in Fig. 18a. To display the patterns clearly, the high-resolution artwork used to mask the metallic patterns is displayed in Fig. 18b, instead of the actual antenna. The RCS and radiation performances of the low-RCS antenna are detailed in the sections that follow.

A. RCS PERFORMANCE

The simulated and measured monostatic RCS patterns are displayed in Fig. 19; an excellent agreement is indicated. The RCS, along the specular direction under normal incidence,
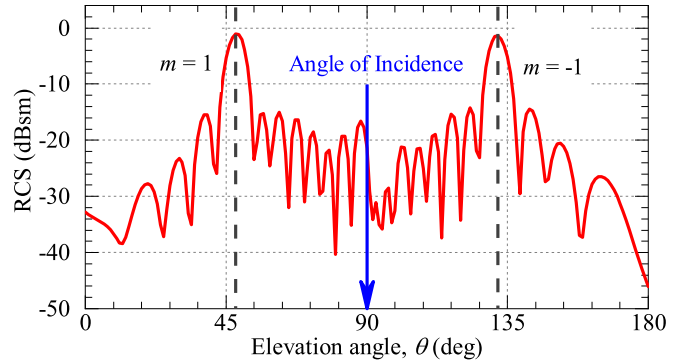

FIGURE 20. The simulated bistatic RCS pattern pertaining to the fabricated square-wave modulated LWA. The two main lobes correspond to the $m = \pm 1$ diffraction modes, while the RCS along the specular direction is reduced by the square-wave modulation.

of a sinusoidally-modulated LWA with the same geometry and modulation parameters is about -0.96 dBsm, as shown in Fig. 12; the RCS is reduced to about -21 dBsm (an RCS reduction of 20 dB) using square-wave modulation. The aperture of the LWA is along the *x-y* plane for polar plots while, for all the other figures, the *z*-axis is along the length of the antenna. It can be observed from Fig. 19 that for an incident angle of 30°, which is the direction of the fan beam formed by the antenna, the monostatic/backscattered RCS is -14 dBsm.

The simulated bistatic RCS pattern of the square-wave modulated LWA is displayed in Fig. 20. Comparing this figure to Fig. 12, it can be seen that the lobes corresponding to the $m = \pm 1$ diffraction modes occur at the same elevation angles, as the modulation period is the same. While the amplitude of the lobes pertaining to the $m = \pm 1$ diffraction modes remains the same, the lobe corresponding to the $m = 0$ diffraction mode (specular direction) is canceled, which can be interpreted using the array theory-based analytical model discussed in Section III-A. A null is formed in the element factor along the specular direction, due to the 180° reflection phase difference between the half-periods; this can also be interpreted using the generalized Snell's law of reflection.

B. RADIATION PERFORMANCE

The measured radiation pattern is compared to simulations in Fig. 21. The simulated and measured patterns are in excellent agreement. A maximum gain of 16.7 dBi is measured at the desired angular direction of 30° from broadside; this corresponds to an aperture efficiency of 18%. The radiated far-fields are vertically (E_θ) polarized, as the metasurface has an inductive surface-reactance profile, and it uses TM-polarized leaky-waves. The cross-polarization level is about -38 dB, as shown in Fig. 22.

Two major sidelobes are formed by the $n = -1$ Floquet mode of the third Fourier harmonic and the $n = -2$ Floquet mode pertaining to the fundamental Fourier harmonic. From (6), the angular directions of the sidelobes
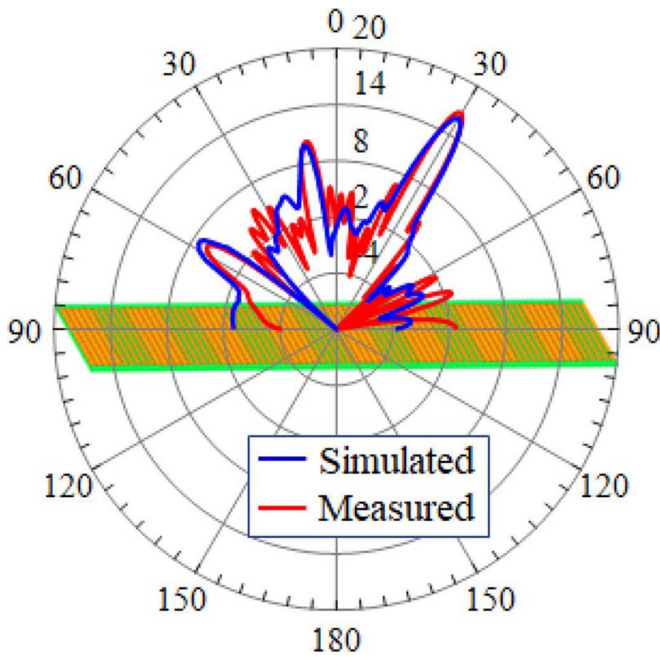
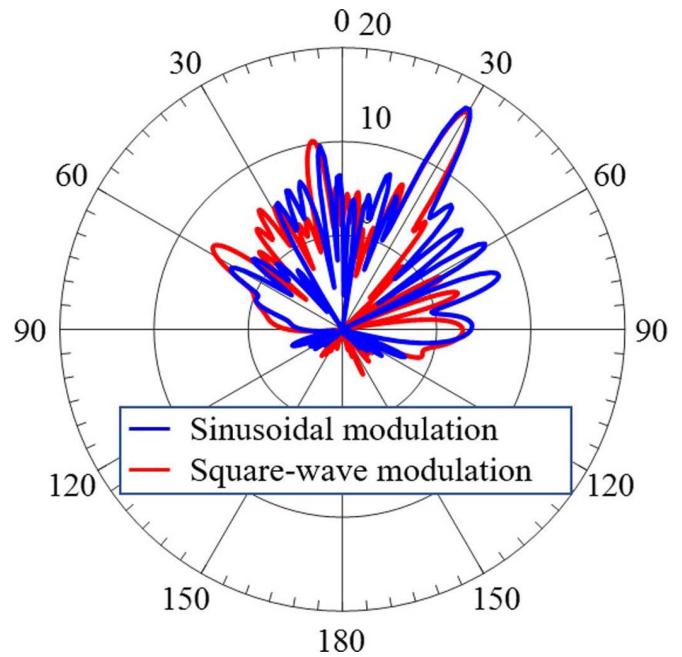**FIGURE 21.** The comparison between the simulated and measured E-plane radiation patterns at 15 GHz.

FIGURE 23. The comparison between the measured E-plane radiation patterns at 15 GHz for sinusoidally-modulated and checkerboard LWAs.
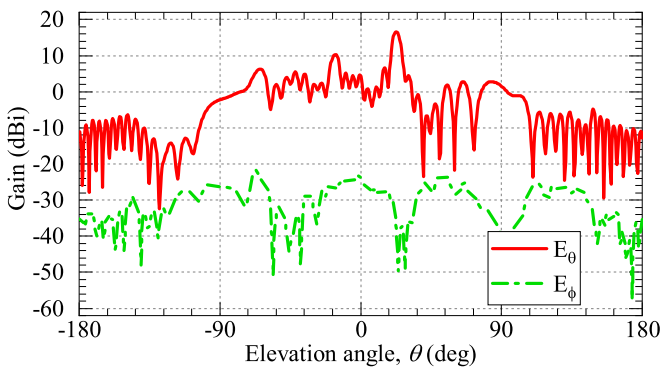

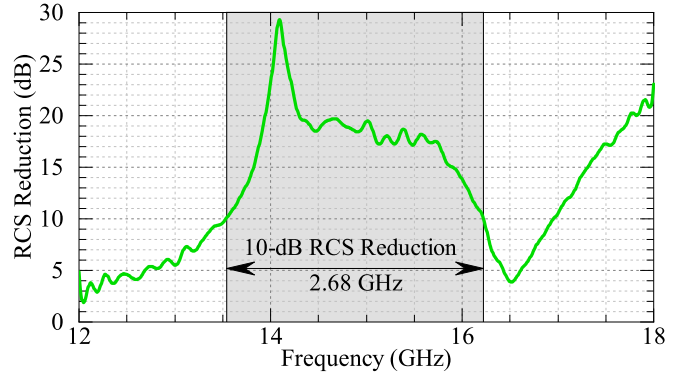**FIGURE 22.** The measured co-polarization and cross-polarization E-plane radiation patterns.

FIGURE 24. The measured RCS reduction is plotted against the operating frequency and the 10-dB RCS reduction bandwidth is highlighted in gray.

from broadside are along $-9.62°$ and $-56.5°$. The predicted directions of the sidelobes accurately match the simulations and measurements shown in Fig. 21. The sidelobe level of the fabricated prototype is about -6.5 dB, which could be undesirable for some applications. The sidelobe level can be decreased by reducing the modulation index, which decreases the reflection phase difference between the half-periods; this results in an increased RCS. Hence, there is a trade-off between the sidelobe level and RCS reduction.

It should also be noted that, for the same geometry, the sidelobe level corresponding to sine-wave modulation is -7.5 dB. Hence, the square-wave modulation increases the sidelobe level by 1 dB, as shown in Fig. 23. For a 1 dB increase of the sidelobe level, the RCS of the antenna is reduced by 20 dB; this is a very good trade-off for RCS reduction.

C. OPERATION BANDWIDTH

The measured normal incidence RCS reduction, at a frequency range of 12 GHz to 18 GHz, is plotted in Fig. 24. RCS reduction of 10 dB or more, relative to a sinusoidally-modulated LWA, is obtained for 13.54 - 16.22 GHz; this corresponds to a fractional bandwidth of 18%. The RCS-reduction bandwidth is limited by the frequency-dependent nature of the reflection phase of the metasurface. The bandwidth can be improved by using metasurface unit cells with multiple resonances [30].

The designed LWA employs forward leaky waves, and as the operating frequency increases, the formed fan beam tilts towards the end-fire direction. The operation bandwidth of the antenna can be defined as the bandwidth within which the peak gain is not reduced by more than 3 dB. The plot of the measured peak gain of the metasurface LWA, at a frequency range of 14 GHz to 16.5 GHz, is displayed in Fig. 25. It
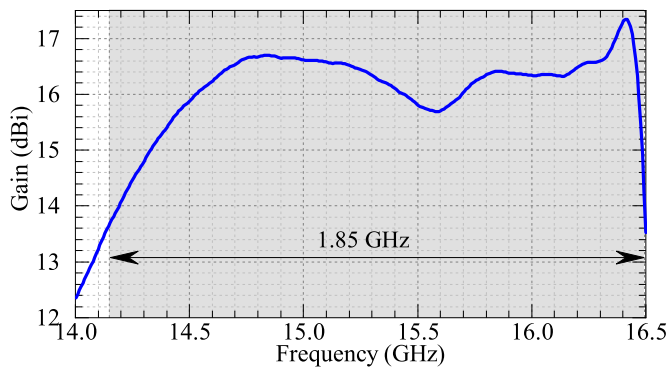
FIGURE 25. The measured peak gain is plotted against the operating frequency and the 3-dB gain bandwidth is highlighted in gray.

is observed that the 3-dB gain bandwidth corresponds to 14.15 GHz - 16.5 GHz; this can be increased further by employing multiple dielectric layers [39].

Within the operation bandwidth, the low-RCS LWA needs to satisfy the requirements related to both the RCS and radiation performances. Hence, the operation bandwidth of the designed metasurface LWA is 14.15 GHz - 16.22 GHz.

VI. CONCLUSION

A new class of metasurface leaky-wave antennas with inherently low monostatic RCS is proposed. Contrary to the existing RCS reduction techniques, the monostatic RCS of the LWAs, for normal incidence parallel polarization, is reduced without increasing the overall area or the thickness of the structure. The RCS reduction is achieved by modulating the surface reactance with a square wave.

The radiation characteristics of the LWAs are analyzed by expressing the square-wave as a superposition of Fourier harmonics and expanding each harmonic as a sum of an infinite number of Floquet modes. An analytical expression for the far-zone radiated fields is derived, and it is shown that the sidelobe level increases drastically with the modulation index.

The RCS of the square-wave modulated LWAs is predicted by modeling the antenna as an array, where each modulation period corresponds to an array element. The normalized element factor is derived using physical optics, and the pattern is denormalized by determining the magnitude of the reflection coefficient as the energy coupled to the $m = 0$ diffraction mode using Floquet simulations on an array element. The reflection phase difference needed to achieve a 10-dB RCS reduction is $180° \pm 25.5°$.

The impact on the modulation parameters on both the radiation and scattering characteristics is analyzed to design the low-RCS metasurface LWA. It is shown that larger values of average surface reactance, modulation period and the modulation index are required to achieve the reflection phase difference. However, to form the beam in the desired direction, the required modulation period decreases when X_a increases. Moreover, it is shown that a small modulation index is preferred to maintain a low sidelobe level. Taking

the above trade-offs into consideration, a low-RCS LWA was designed, fabricated and measured. An RCS reduction of 20 dB was achieved relative to a sinusoidally-modulated LWA with the same geometry, average surface reactance and modulation period. The gain and the sidelobe level of the fabricated antenna were measured to be 16.7 dBi and −6.5 dB, respectively. The sidelobe level can be reduced by compromising the RCS reduction. The bandwidth of the low-RCS LWA is 14.15 - 16.22 GHz.

REFERENCES

[1] S. S. Bukhari, J. Y. Vardaxoglou, and W. Whittow, "A metasurfaces review: Definitions and applications," *Appl. Sci.*, vol. 9, no. 13, p. 2727, 2019.

[2] A. A. Oliner and A. Hessel, "Guided waves on sinusoidally-modulated reactance surfaces," *IRE Trans. Antennas Propag.*, vol. 7, no. 5, pp. 201–208, Dec. 1959.

[3] M. V. Kuznetsov, V. G.-G. Buendía, Z. Shafiq, L. Matekovits, D. E. Anagnostou, and S. K. Podilchak, "Printed leaky-wave antenna with aperture control using width-modulated microstrip lines and TM surface-wave feeding by SIW technology," *IEEE Antennas Wireless Propag. Lett.*, vol. 18, no. 9, pp. 1809–1813, Sep. 2019.

[4] G. Minatti *et al.*, "Modulated metasurface antennas for space: Synthesis, analysis and realizations," *IEEE Trans. Antennas Propag.*, vol. 63, no. 4, pp. 1288–1300, Apr. 2015.

[5] S. Ramalingam, C. A. Balanis, C. R. Birtcher, S. Pandi, and H. N. Shaman, "Axially modulated cylindrical metasurface leaky-wave antennas," *IEEE Antennas Wireless Propag. Lett.*, vol. 17, no. 1, pp. 130–133, Jan. 2018.

[6] T. Zvolensky, J. N. Gollub, D. L. Marks, and D. R. Smith, "Design and analysis of a W-band metasurface-based computational imaging system," *IEEE Access*, vol. 5, pp. 9911–9918, 2017.

[7] A. M. Patel and A. Grbic, "A printed leaky-wave antenna based on a sinusoidally-modulated reactance surface," *IEEE Trans. Antennas Propag.*, vol. 59, no. 6, pp. 2087–2096, Jun. 2011.

[8] B. H. Fong, J. S. Colburn, J. J. Ottusch, J. L. Visher, and D. F. Sievenpiper, "Scalar and tensor holographic artificial impedance surfaces," *IEEE Trans. Antennas Propag.*, vol. 58, no. 10, pp. 3212–3221, Oct. 2010.

[9] S. Pandi, C. A. Balanis, and C. R. Birtcher, "Design of scalar impedance holographic metasurfaces for antenna beam formation with desired polarization," *IEEE Trans. Antennas Propag.*, vol. 63, no. 7, pp. 3016–3024, Jul. 2015.

[10] G. Minatti, F. Caminita, M. Casaletti, and S. Maci, "Spiral leaky-wave antennas based on modulated surface impedance," *IEEE Trans. Antennas Propag.*, vol. 59, no. 12, pp. 4436–4444, Dec. 2011.

[11] G. Minatti, F. Caminita, E. Martini, M. Sabbadini, and S. Maci, "Synthesis of modulated-metasurface antennas with amplitude, phase, and polarization control," *IEEE Trans. Antennas Propag.*, vol. 64, no. 9, pp. 3907–3919, Sep. 2016.

[12] S. Ramalingam, C. A. Balanis, C. R. Birtcher, and H. N. Shaman, "Polarization-diverse holographic metasurfaces," *IEEE Antennas Wireless Propag. Lett.*, vol. 18, no. 2, pp. 264–268, Feb. 2019.

[13] D. Sievenpiper *et al.*, "Holographic artificial impedance surfaces for conformal antennas," in *IEEE Antennas Propag. Soc. AP-S Int. Symp. Dig.*, vol. 1, 2005, pp. 256–259.

[14] J. L. Gómez-Tornero, "Analysis and design of conformal tapered leaky-wave antennas," *IEEE Antennas Wireless Propag. Lett.*, vol. 10, pp. 1068–1071, 2011.

[15] S. Pandi, C. A. Balanis, and C. R. Birtcher, "Curvature modeling in design of circumferentially modulated cylindrical metasurface LWA," *IEEE Antennas Wireless Propag. Lett.*, vol. 16, pp. 1024–1027, 2017.

[16] A. Diaz-Rubio, V. S. Asadchy, A. Elsakka, and S. A. Tretyakov, "From the generalized reflection law to the realization of perfect anomalous reflectors," *Sci. Adv.*, vol. 3, no. 8, 2017, Art. no. e1602714.

[17] A. Hessel and A. A. Oliner, "A new theory of wood's anomalies on optical gratings," *Appl. Opt.*, vol. 4, no. 10, pp. 1275–1297, 1965.

[18] C. Vasanelli, F. Bögelsack, and C. Waldschmidt, "Reducing the radar cross section of microstrip arrays using AMC structures for the vehicle integration of automotive radars," *IEEE Trans. Antennas Propag.*, vol. 66, no. 3, pp. 1456–1464, Mar. 2018.

[19] Y. Liu, Y. Hao, K. Li, and S. Gong, "Wideband and polarization-independent radar cross section reduction using holographic metasurface," *IEEE Antennas Wireless Propag. Lett.*, vol. 15, pp. 1028–1031, 2016.

[20] Y. Liu and X. Zhao, "Perfect absorber metamaterial for designing low-RCS patch antenna," *IEEE Antennas Wireless Propag. Lett.*, vol. 13, pp. 1473–1476, 2014.

[21] C. Huang, W. Pan, X. Ma, and X. Luo, "Wideband radar cross-section reduction of a stacked patch array antenna using metasurface," *IEEE Antennas Wireless Propag. Lett.*, vol. 14, pp. 1369–1372, 2015.

[22] Y. Liu, Y. Hao, H. Wang, K. Li, and S. Gong, "Low RCS microstrip patch antenna using frequency-selective surface and microstrip resonator," *IEEE Antennas Wireless Propag. Lett.*, vol. 14, pp. 1290–1293, 2015.

[23] S. Genovesi, F. Costa, and A. Monorchio, "Low-profile array with reduced radar cross section by using hybrid frequency selective surfaces," *IEEE Trans. Antennas Propag.*, vol. 60, no. 5, pp. 2327–2335, May 2012.

[24] C. Huang, W. Pan, X. Ma, and X. Luo, "A frequency reconfigurable directive antenna with wideband low-RCS property," *IEEE Trans. Antennas Propag.*, vol. 64, no. 3, pp. 1173–1178, Mar. 2016.

[25] K. Li, Y. Liu, Y. Jia, and Y. J. Guo, "A circularly polarized high-gain antenna with low RCS over a wideband using chessboard polarization conversion metasurfaces," *IEEE Trans. Antennas Propag.*, vol. 65, no. 8, pp. 4288–4292, Aug. 2017.

[26] W. Xu, J. Wang, M. Chen, Z. Zhang, and Z. Li, "A novel microstrip antenna with composite patch structure for reduction of in-band RCS," *IEEE Antennas Wireless Propag. Lett.*, vol. 14, pp. 139–142, 2015.

[27] K. Kandasamy, B. Majumder, J. Mukherjee, and K. P. Ray, "Low-RCS and polarization-reconfigurable antenna using cross-slot-based metasurface," *IEEE Antennas Wireless Propag. Lett.*, vol. 14, pp. 1638–1641, 2015.

[28] C. M. Dikmen, S. Çimen, and G. Çakır, "Planar octagonal-shaped UWB antenna with reduced radar cross section," *IEEE Trans. Antennas Propag.*, vol. 62, no. 6, pp. 2946–2953, Jun. 2014.

[29] W. Pan, C. Huang, P. Chen, X. Ma, C. Hu, and X. Luo, "A low-RCS and high-gain partially reflecting surface antenna," *IEEE Trans. Antennas Propag.*, vol. 62, no. 2, pp. 945–949, Feb. 2014.

[30] W. Chen, C. A. Balanis, and C. R. Birtcher, "Checkerboard EBG surfaces for wideband radar cross section reduction," *IEEE Trans. Antennas Propag.*, vol. 63, no. 6, pp. 2636–2645, Jun. 2015.

[31] D. González-Ovejero, G. Minatti, G. Chattopadhyay, and S. Maci, "Multibeam by metasurface antennas," *IEEE Trans. Antennas Propag.*, vol. 65, no. 6, pp. 2923–2930, Jun. 2017.

[32] C. A. Balanis, *Antenna Theory: Analysis and Design*, 4th ed. Hoboken, NJ, USA: Wiley, 2016.

[33] S. Ramalingam, C. A. Balanis, C. R. Birtcher, S. Pandi, and H. N. Shaman, "Bistatic RCS of a one-dimensional metasurface leaky-wave antenna," in *Proc. IEEE Int. Symp. Antennas Propag. (USNC/URSI) Nat. Radio Sci. Meeting*, Atlanta, GA, USA, 2019, pp. 621–622.

[34] A. Wirgin, "Scattering from sinusoidal gratings: An evaluation of the Kirchhoff approximation," *J. Opt. Soc. Amer.*, vol. 73, no. 8, pp. 1028–1041, 1983.

[35] D. Sievenpiper, "High-impedance electromagnetic surfaces," Ph.D. dissertation, Elect. Eng., Univ. California at Los Angeles, Los Angeles, CA, USA, 1999.

[36] S. Maci, G. Minatti, M. Casaletti, and M. Bosiljevac, "Metasurfing: Addressing waves on impenetrable metasurfaces," *IEEE Antennas Wireless Propag. Lett.*, vol. 10, pp. 1499–1502, 2011.

[37] M. Alyahya, C. A. Balanis, C. R. Birtcher, H. N. Shaman, and W. A. Alomar, "Physical optics modeling of scattering by checkerboard structure for RCS reduction," in *Proc. IEEE Int. Symp. Antennas Propag. (USNC-URSI) Radio Sci. Meeting*, Atlanta, GA, USA, 2019, pp. 1693–1694.

[38] C. A. Balanis, *Advanced Engineering Electromagnetics*, 2nd ed. Hoboken, NJ, USA: Wiley, 2012.

[39] S. Ramalingam, C. A. Balanis, C. R. Birtcher, and H. N. Shaman, "Multilayered axially modulated cylindrical metasurfaces," in *Proc. IEEE Int. Symp. Antennas Propag. (USNC/URSI) Nat. Radio Sci. Meeting*, Boston, MA, USA, 2018, pp. 967–968.
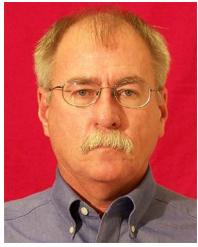
SUBRAMANIAN RAMALINGAM (Member, IEEE) received the Bachelor of Technology degree in electronics and communication engineering from Amrita Vishwa Vidyapeetham, Coimbatore, India, in 2012, and the Master of Science in Engineering degree in electrical engineering from Arizona State University, Tempe, AZ, USA, in 2014, where he is currently pursuing the Ph.D. degree in electrical engineering.

He worked as an Applications Engineering Intern in 2013 and the Radar Product Engineer with NXP (Freescale) Semiconductors, Chandler, AZ, USA, from 2014 to 2016. He also worked as an Antenna Design Engineering Intern with Apple Inc., Cupertino, CA, USA, in 2019. His research interests are antennas, metasurfaces, and electromagnetic theory.

CONSTANTINE A. BALANIS (Life Fellow, IEEE) received the B.S.E.E. degree from Virginia Tech, Blacksburg, VA, USA, in 1964, the M.S.E.E. degree from the University of Virginia, Charlottesville, VA, USA, in 1966, the Ph.D. degree in electrical engineering from Ohio State University, Columbus, OH, USA, in l969, and the Honorary Doctorate degree from the Aristotle University of Thessaloniki in 2004.

From 1964 to 1970, he was with NASA Langley Research Center, Hampton, VA, USA. From 1970 to 1983, he was with the Department of Electrical Engineering, West Virginia University, Morgantown, WV, USA. Since 1983, he has been with the School of Electrical, Computer and Energy Engineering, Arizona State University, Tempe, AZ, USA, where he is a Regents' Professor. He has authored *Antenna Theory: Analysis and Design* (Wiley, 1982, 1997, 2005, 2016), *Advanced Engineering Electromagnetics* (Wiley, 1989, 2012), and *Introduction to Smart Antennas* (Morgan and Claypool, 2007), and an Editor of *Modern Antenna Handbook* (Wiley, 2008), *Series on Antennas and Propagation* (Morgan & Claypool), and *Series on Computational Electromagnetics* (Morgan & Claypool). His research interests are in computational electromagnetics, flexible antennas and high impedance surfaces, smart antennas, and multipath propagation. He received the 2017 IEEE MTT Rudolf Henning Distinguished Mentoring Award, the 2014 James R. James, Lifetime Achievement Award, LAPC, Loughborough, U.K., the 2012 Distinguished Achievement Award of the IEEE Antennas and Propagation Society, the 2012 Distinguished Achievement Alumnus Award (College of Engineering, The Ohio State University), the 2005 Chen-To Tai Distinguished Educator Award of the IEEE Antennas and Propagation Society, the 2000 IEEE Millennium Award, the 1996 Graduate Mentor Award of Arizona State University, the 1992 Special Professionalism Award of the IEEE Phoenix Section, the 1989 Individual Achievement Award of the IEEE Region 6, and the 1987–1988 Graduate Teaching Excellence Award, School of Engineering, Arizona State University. He has served as an Associate Editor for the IEEE TRANSACTIONS ON ANTENNAS AND PROPAGATION from 1974 to 1977 and the IEEE TRANSACTIONS ON GEOSCIENCE AND REMOTE SENSING from 1981 to 1984; as an Editor for the Newsletter for the IEEE Geoscience and Remote Sensing Society from 1982 to 1983; as the Second Vice-President in 1984, a member of the Administrative Committee of the IEEE Geoscience and Remote Sensing Society from 1984 to 1985; the Chair for the Distinguished Lecturer Program from 1988 to 1991, a member of the AdCom from 1992 to 1995 and from 1997 to 1999, the Distinguished Lecturer from 2003 to 2005, and the Chair for the Awards and Fellows Committee of the IEEE Antennas and Propagation Society from 2009 to 2011.

CRAIG R. BIRTCHER received the B.S.E.E. and M.S.E.E. degrees in electrical engineering from Arizona State University, Tempe, AZ, USA, in 1983 and 1992, respectively. Since 1987, he has been with Arizona State University, where he is currently an Associate Research Professional in charge of the Electromagnetic Anechoic Chamber Facility. His research interests include antenna and RCS measurement techniques and near-field to far-field methods.

SIVASEETHARAMAN PANDI (Member, IEEE) received the Bachelor of Technology degree in electronics and communications engineering from Amrita Vishwa Vidyapeetham, Coimbatore, India, in 2009, the Master of Science degree in electrical engineering from Northern Illinois University, DeKalb, IL, USA, in 2011, and the Ph.D. degree from Arizona State University, Tempe, AZ, USA, in 2017. His research interests include high impedance surfaces, planar leaky wave antennas, and microwave circuits.